Supplement of Atmos. Chem. Phys., 16, 10175–10194, 2016
http://www.atmos-chem-phys.net/16/10175/2016/
doi:10.5194/acp-16-10175-2016-supplement

Atmospheric Chemistry and Physics Open Access EGU

Supplement of

The contribution of soil biogenic NO and HONO emissions from a managed hyperarid ecosystem to the regional NO_x emissions during growing season

Buhalqem Mamtimin et al.

Correspondence to: Buhalqem Mamtimin (buhalqem.mamtimin@mpic.de)

S1. Development of the Geoscience General Tool Package (GGTP)

In order to upscale biogenic NO emissions derived from laboratory measurements to the oasis level, we have developed a tool, the so-called "Geoscience General Tool Package (GGTP)" for ARCGIS 10.x using the model builder and python 2.7. By knowing LST, SMI and the land-use-type specific parameterized soil biogenic NO fluxes for each field, the net NO fluxes of each pixel of the oasis were calculated in a fine scale matrix (30x30 m²) within the GGTP framework. For that, GGTP has been specifically developed, namely to process digital images (e.g. Landsat images) and to model 2D distributions of biogenic NO emission. In particular, the following calculation (sub-) schemes have been implemented (see S1-S9).

S1.1 Landsat-7 SLC-off gap filling

The Landsat 7 Enhanced Thematic Mapper Plus (ETM+) scan line corrector (SLC) failed on May 31, 2003, causing the scanning patterns exhibited wedge-shaped, scan-to-scan gaps. The ETM+ has continued to acquire data with the SLC powered off, leading to images that are missing approximately 22% of the usual scene area. Therefore, the U.S. Geological Survey (USGS) provided an additional bit mask (gap files) that identifies the location of the image gaps. We used a local linear histogram matching radiometric algorithm to create a gap-filled output product (Beck, 2003; Storey et al, 2005; Storey, 2011). This technique was proposed by USGS/NASA and consists of a localized linear transformation performed in a moving window. The implementation of this algorithm requires both image products, SCL-off and SCL-on scenes. For that, we used the Landsat ETM+ SCL-on scene of August 2000. The gap filling was implemented by calculation of (a) the gain and bias, based on the mean and standard deviation of common pixels, and (b) the missing pixel value, using the derived gain and bias as shown by Beck (2003), Storey et al. (2005, 2011) and Chen et al. (2011).

S1.2 Calculation of NDVI Surfaces ($NDVI_{surf}$)

The NDVI differentiates between the green vegetation and soil background, which is useful for the retrievals of land surface emissivity and soil moisture (Van de Griend et al., 1993; Jackson et al., 2004; Wang et al., 2007; Yilmaz et al., 2008). Erroneous NDVI estimates can directly affect biophysical parameters such as temperature and moisture which are extracted directly and indirectly from these values; thus, pre-processing of atmospheric corrections of remotely sensed data is essential (Jensen, 2005). One of these atmospheric corrections is the absolute radiometric correction which aims to turn the raw digital numbers (DN), recorded by a remote sensing instrument for scaled surface reflectance values (Du et al., 2002; Jensen,

2005). The NDVI can be calculated from Landsat image bands ETM 3 and ETM 4 (near-infrared and red); in this study atmospheric corrections for bands ETM3 and ETM4 were. The calculated NDVI values, which are then representing natural surfaces, are called $NDVI_{surf}$ (Sobrino et al., 2004).

S1.3 At-sensor spectral radiance (L_λ)

The at-sensor spectral radiance (L_λ) is used to characterize the amount of light at the sensor and it is a scientific term used to describe the power of radiation. The calculation of L_λ is a primary step in converting image data from multiple sensors into a common physical scale which can be implemented by radiometric calibration. During this calibration process, raw DN transmitted from the satellite instrument converted to calibrate DN (Q_{cal}). DN of Landsat images represents the dimensionless integer that a satellite uses to record relative amounts of radiance. For radiometric calibration, the following steps were involved: (a) pixel values of DN are converted into absolute spectral radiance by using a 32-bit floating point calculation, (b) absolute radiances are then scaled to 8-bit values representing calibrated DN Q_{cal}, and (c) the conversion of Q_{cal} products back to at-sensor spectral radiance (L_λ). For conversion of Q_{cal} to L_λ, the following equation is used (Chander and Markham, 2003):

$$L_\lambda = (L_{max\lambda} - L_{min\lambda} / Q_{calmax}) \times Q_{cal} + L_{min\lambda} \quad (S1)$$

where L_λ is the spectral radiance at the sensor (power per steradian, μm and m², i.e. W m^{-2} sr^{-1} μm^{-1}), Q_{cal} is the calibrated pixel value (dimensionless), and Q_{calmax} is the maximum calibrated pixel value (corresponding to $L_{max\lambda}$), $L_{max\lambda}$ and $L_{min\lambda}$ (W m^{-2} sr^{-1} μm^{-1}) are the spectral radiances scaled to Q_{calmax} and Q_{calmin}, respectively. The lower and upper limit rescaling factors ($L_{max\lambda}$ and $L_{min\lambda}$) were obtained from the supplemented header file of the satellite images.

S1.4 Top of atmosphere (TOA) reflectance (ρ_{TOA})

To obtain *NDVI* values, the calculated radiances need to be converted into an at-sensor reflectance (spectral reflectance value), also called top of atmosphere reflectance (ρ_{TOA}). The top of atmosphere (TOA) correction converts the at-sensor spectral radiance (L_λ) to the top of atmosphere reflectance (ρ_{TOA}), and this process is one of the atmospheric correction methods used to reduce scene-to-scene variability (Markham and Barker, 1986; Chander and Markham, 2003; Chander et al., 2009). This is important when comparing scenes to scenes or producing image mosaics. The dimensionless TOA reflectance, called ρ_{TOA}, is defined as follows:

$$\rho_{TOA} = \frac{\pi * L_\lambda * d^2}{E_{SUN,\lambda} * \cos(\theta_s)} \quad (S2)$$

where L_λ is the spectral radiance at the sensor (s. eq. (1)), d is the Earth-Sun distance [astronomical units] depending on the day of the year (DOY), $E_{SUN,\lambda}$ is the mean exo-atmospheric solar irradiance (W m^{-2} μm^{-1}), and $cos(\theta_s)$ is the cosine of the sun zenith angle, which is equal to sine of the solar elevation angle. The solar elevation angle at each Landsat scene center is typically stored in the Level 1 product header file of each Landsat Image (obtained from USGS Earth Explorer or GloVis online interfaces under the respective scene metadata).

S1.5 At-surface reflectance (ρ_{surf})

Basically, it is possible to derive the NDVI from the at sensor corrected reflectance (ρ_{TOA}), which is then called $NDVI_{TOA}$ (Sobrino, et al. 2004). However, the *NDVI* is based on surface reflectance, thus, it is more accurate to convert the at-sensor reflectance (TOA) into the at-surface reflectance. Then, the estimated *NDVI* values would represent the natural surface, and are called $NDVI_{surf}$. As described by Sobrino et al. (2004), the at-surface reflectance is:

$$\rho_{surf}^{ETM\,3} = 1.0705 \times \rho_{TOA}^{ETM\,3} - 0.0121 \quad (S3a)$$

$$\rho_{surf}^{ETM\,4} = 1.0805 \times \rho_{TOA}^{ETM\,4} - 0.0047 \quad (S3b)$$

where $\rho_{surf}^{ETM\,3}$ and $\rho_{surf}^{ETM\,4}$ are the at-surface reflectivities, and $\rho_{TOA}^{ETM\,3}$, $\rho_{TOA}^{ETM\,4}$ are the corresponding TOA reflectivities for the ETM band 3 and ETM band 4, respectively, calculated by eq. (S2).

$NDVI_{surf}$ is then calculated as follows:

$$NDVI_{surf} = (\rho_{surf}^{ETM\,4} - \rho_{surf}^{ETM\,3}) / (\rho_{surf}^{ETM\,4} + \rho_{surf}^{ETM\,3}) \quad (S4)$$

Theoretically, $NDVI_{surf}$ values, which constitute a ratio, range from -1 to 1; water typically has an *NDVI* value less than 0, bare soils range between 0 and 0.1 and vegetation is represented by *NDVI* >0.1.

S1.6 Land surface emissivity and land surface temperature T_s

Knowledge of the land surface emissivity is highly indispensable to retrieve the land surface temperature (T_s) and soil moisture index (*SMI*) from remotely sensed data. Land surface emissivity (ε) is known as the relative fraction of a surface emission compared to the emission of a black body at the same temperature. As the land cover varies greatly from place to place,

land surface emissivity (LSE) widely varies from one location to another. Van de Griend and Owe (1993) found a high correlation between measured emissivity and *NDVI* obtained from red and near-infrared (NIR) spectral reflectance, expressed by the following relation:

$$\varepsilon = 1{,}0094 + 0{,}047 \ln NDVI_{surf} \qquad (S5)$$

Note, that this relationship is not valid for areas characterized by highly dense vegetation cover. Since the *NDVI* values in our study area range between 0 and 0.7, application of eq. (5) is certainly justified in the case of the Tohsun oasis. For the calculation of LST we made use of Stefan-Boltzmann's law:

$$B = \varepsilon \sigma T_S^4 = \sigma T_B^4 \qquad (S6)$$

where, B is the total amount of the emitted radiation (W m^{-2}), ε is the land surface emissivity (obtained from eq.(S5)), σ is the Stefan-Boltzmann constant (5,67 x 10^{-8} Wm^{-2} K^{-4}), and T_S and T_B are the land surface temperature and the at-sensor brightness temperature (K).

Therefore the land surface temperature T_s is defined as:

$$T_S = \frac{1}{\varepsilon^{0,25}} T_B \qquad (S7)$$

The at-sensor brightness temperature can be calculated from the satellite image's thermal band of high gain mode (band 6.2). In the case of Landsat satellite series, Schott and Volchok (1985), Markham and Barker (1986), Irish (2003) and Chander et al. (2009) used a simplified formula for the estimation of the at-sensor brightness temperature as follows:

$$T_B = \frac{K2}{\ln\left(\frac{K1}{L_\lambda} + 1\right)} \qquad (S8)$$

Here *K1* (W m^{-2} sr^{-1} μm^{-1}) and *K2* (K) are calibration constants, and L_λ the spectral radiance at the sensor's aperture. For Landsat-7 ETM+ images, *K1* and *K2* have numerical values of 666.09 and 1282.71, respectively.

Generally, T_s is defined as the so-called "skin temperature" of the surface. For the bare soil surface, it is the soil temperature; for the vegetated areas, T_s can be considered as the average temperature of the vegetation body and the soil surface below the vegetation.

The development of the Geoscience General Tool Package and its application to Landsat images allowed us to present maps of the 2D distribution of Tohsun oasis' land surface temperature for the begin, the middle, and the end of the 2010 vegetation period, i.e., on 25 April; 28 July, 13 August, 21 August; 06 September and 22 September, respectively. Results are shown in Fig. S1. Cultivated parts of the oasis are sharply separated from the surrounding

desert, related land surface temperature differences exceed 10 K for all growth stages. However, significant temperature differences were also observed between cotton and grape fields, particularly in July; here, land surface temperatures were 35–55 °C in grape fields, and 25–50 °C in the cotton fields. Lower skin temperatures of the cotton fields were due to (a) effective shading of the soil by the fully developed cotton canopy which is considerably more dense than that of the grapes, and (b) transpiration of the cotton leaves which are known for highest transpiration rates.

S1.7 T_s–$NDVI_{surf}$ scatter space and Soil Moisture Index (SMI)

In several studies (Goward et al., 2002; Lambine and Ehrlich, 1996; Sandholt et al., 2002; Wang et al., 2007), the correlation between T_s and *NDVI* has been shown to be related to surface soil moisture. Several approaches were tested to develop and improve soil moisture estimates from the space of T_s and *NDVI* (Carlson et al., 1995; Roy, 1997; Goward et al., 2002; Sandholt et al., 2002; Zeng et al., 2004). In this space, land surface temperature T_S is determined by the soil thermal inertia (Lambin and Ehrlich, 1996) which is based on the assumption, that the remotely sensed surface temperatures are related to *NDVI,* and that *NDVI* is determined by land surface reflectance. The emitted heat flux from a vegetated area is lower than that from the bare soil due to stomatal transpiration of the vegetation and lower thermal inertia within the vegetation (Lambin and Ehrlich, 1996; Sandholt et al., 2002). Therefore, T_s is dependent on both, the thermal inertia and the available moisture of vegetation. This relation is ideally represented in a triangle shape, when $NDVI_{surf}$ data are plotted *vs.* corresponding T_S data (s. Fig. 2). The lower line which envelopes the triangle shaped scatter plot represents the so-called "wet edge", while the upper, negatively sloped line represents the so-called "dry edge" of the any given (T_S;$NDVI_{surface}$)-data set.

Zeng et al. (2004) applied this method successfully to arid areas and showed that both linear relationships between T_S and $NDVI_{surface}$ along the dry edge (dry border) and wet edge (wet border) assured that soil moisture could be estimated from a T_S-$NDVI_{surface}$ scatter plot (Fig.2). They defined a soil moisture index (*SMI*) for the T_s-$NDVI_{surface}$ space, whose value is zero along the "dry edge" and equal unity along the "wet edge". The line from point "A" to "C" in Fig. 1 represents the dry edge (dry border) of respective vegetated areas, while the line from point "B" to "C" indicates its wet edge (wet border). According to Zeng et al. (2004), the desired *SMI* value reads as follows:

$$SMI = \frac{T_{s\max} - T_s}{T_{s\max} - T_{s\min}} \quad (S9)$$

where $T_{s\,max}$ and $T_{s\,min}$ are the maximum and minimum surface temperatures in the scatter space for a given pixel, and T_s is the remotely sensed surface temperature at a given pixel for a given $NDVI_{surf}$. According to eq. (S9) *SMI* is the ratio of two temperature differences (for a given pixel); for instance, the value of ($T_{s\,max} - T_s$) at point "D" in Fig. S2 is the temperature difference between point "E" and "D", and the value of ($T_{s\,max} - T_{s\,min}$) is the temperature difference between point "E" and "F".

$T_{s\,max}$ and $T_{s\,min}$ are defined as linear functions of $NDVI_{surface}$ and represent the enveloping lines at the dry border and wet border of the T_s-$NDVI_{surface}$ scatter space:

$$T_{s\max} = a_1 NDVI_{surf} + b_1 \quad (S10a)$$

$$T_{s\min} = a_2 NDVI_{surf} + b_2 \quad (S10b)$$

where a_1, a_2, b_1, *and* b_2 were obtained by linear regression of known remotely sensed data along the dry and wet edges. The *SMI* value for a given data point "D" ($NDVI_{surface,D}$; $T_{S,D}$) is calculated from eq. (S9) using eq. (S10a) and (S10b) to obtain $T_{smax,\,D}$ and $T_{smin,\,D}$.

The Soil Moisture Index (*SMI*) was calculated using the parameters a_1, a_2, b_1, and b_2 which are obtained from linear regression analysis along the dry and wet borders of the triangular T_s–$NDVI_{surface}$ scatter spaces (Fig. S2). To determine the dry and wet edges, the Landsat images of 25 April (begin of the vegetation period), 28 July, 13 August, 21 August (middle of the vegetation period), and 06 September and 22 September (end of the vegetation period) were used. Fig. S3 clearly shows the triangular shape of the scatter plot between $NDVI_{surface}$ (horizontal axis) and T_s (vertical axis). The interpretation of the triangular shape is (Zeng et al., 2004): the more vegetated an area (the higher the $NDVI_{surface}$), the lower the surface temperature. Thus, for a given $NDVI_{surface}$, low T_s values correspond to high amounts of soil moisture (high amounts of *SMI*). The linear relationship between T_S and $NDVI_{surface}$ is in any case statistically significant ($R^2 > 0.7$; s. Fig. S3).

S1.8 Calculation of gravimetric soil moisture contents

The basic concept to convert satellite derived dimensionless SMI data into the volumetric soil moisture content (θ_v) is discussed by Wagner et al. (1999) and Mallick et al. (2009). For that, specific and characteristic soil moisture values for soils of each considered land use type are

needed, preferably those which may correspond to the lower and upper limits of (dimensionless) SMI data (0 and 1).

As a first approximation one may assume as the lower limit for agriculturally managed land use types the volumetric soil moisture content at permanent wilting conditions ("permanent wilting point", *PWP*). The *PWP* is defined as the level at which plants will irreversible, if additional water is not provided; to avoid this, the plants have to be irrigated before the *PWP* is reached. After heavy rain events and after irrigation events soils of vegetated land use types may reach the status of so-called (over-) saturation (flooding irrigation equals to about 10–15cm H_2O column on the soil). However, this status is only observed for about 12–24 h, after the field capacity (*FC*) is equilibrating. Therefore, the soil specific value at conditions of *FC* may be used as upper limit for the volumetric soil moisture content. Soil specific data of *PWP* and *FC* (or for flooding irrigation multiples of *FC*) are typically used in irrigation scheduling, calculation of plant available water, as well as water depth to be applied by irrigation (Diallo and Mariko, 2013). Both limits of volumetric soil moisture content, $\theta_{v,min}$ at *PWP* and $\theta_{v,max}$ at *FC*, are usually determined by standardized laboratory measurements of water tension (*pF*) on undisturbed soil samples ($\theta_{v,max}$ at pF= 1.8; $\theta_{v,min}$ at pF= 4.2). By knowing the corresponding bulk soil densities, volumetric soil moisture contents ($\theta_{v,min}$ and $\theta_{v,max}$) can be converted to gravimetric soil moisture contents ($\theta_{g,min}$ and $\theta_{g,max}$). With $\theta_{g,min}$ and $\theta_{g,max}$ of soil samples from each considered land use type, the corresponding SMI data (dimensionless; ranging from 0 to 1) can be transformed to data of gravimetric soil moisture content (θ_g) by:

$$\theta_{g,} = \theta_{g,min,} + \text{SMI}\ (\theta_{g,max,} - \theta_{g,min}) \qquad (S11)$$

which means SMI=1 at $\theta_{g,max}$ and SMI=0 at $\theta_{g,min}$.

For non-vegetated arid and hyper-arid soils (desert), the lower limit of the volumetric soil moisture content is certainly (much) lower than that at the PWP and the upper limit (at FC) may be reached at best a few hours (days) per year. Therefore, in the case of bare and desert soils, we decided to use for the lower limit value which corresponds to "residual water" of the desiccated soil sample measured by dry mass determination as gravimetrical soil moisture after stopping each incubation experiment in the lab (at pF=6.8). Unfortunately, laboratory measurements of water tension have not been performed on the soil samples from the Tohsun oasis (desert, cotton and grape fields). Land use type specific data for $\theta_{g,min}$ and $\theta_{g,max}$ have been substituted by averages of water tension measurements (at pF= 1.8, 4.2, 6.8) performed on undisturbed soil samples taken around the Taklimakan desert during 2010 (Behrendt et al.,

2014): at 8 desert sites (around the oases of Awati, Kuche, Milan, Mingfeng, Qiemo, Ruoqiang, Sache, and Waxxari), at 7 cotton field sites (within the oases of Awati, Kuche, Milan, Qiemo, Sache, Waxxari), and at 3 jujube plantation sites (within the oases of Milan, Minfeng, Qiemo); grapes and jujube both of them belong to the bushy agricultural landscape type and jujube has the similar height and distance in rows as the grapes. And they have similar water requirements and percent ground cover by their canopy. Thus, we expected the similar availability of water in the soil profile so that similar *FC* and *PWP* for grapes and jujube.

Applying the Geoscience General Tool Package to Landsat images provides spatially high resolved data of the Soil Moisture Index (*SMI*). Using a few straightforward assumptions and the results of laboratory measurements of a few related physical soil data for scaling, *SMI*-values could be converted to corresponding gravimetric soil moisture data. That allowed us to present maps of the 2D distribution of Tohsun oasis' gravimetric soil moisture for the begin, the middle, and the end of the 2010 vegetation period, i.e., on 25 April; 28 July, 13 August, 21 August; 06 September and 22 September, respectively. Results are shown in Fig. S5. In all cases, gravimetric soil moisture contents of the cultivated parts of Tohsun oasis (0.085–0.33) were significantly higher than those of the surrounding desert (0.0028). With respect to the growth stage of Tohsun oasis' vegetation, lowest soil moisture contents (0.085–0.18) have been observed at the beginning of the growing period (April); highest values have been identified in July and August (0.33). Throughout the growing period there was less difference between the gravimetric soil moisture content in the cotton and the grape fields. Particularly in July, the grapes fields seem to have stored similar amounts of available water to the cotton fields: corresponding θ_g–values of cotton fields were between 0.167−0.33, and between 0.085−0.25 for the grape fields.

S1.9 Two dimensional soil NO emission model

The areal distribution of land-cover is shown in Fig. 5 (in sec. 3.1.3). Five land-cover types, shown in a land-cover raster map (30x30m), were identified, namely cotton fields, grape fields, other vegetation, buildings/residential areas, and desert. Based on these results, the dominant land cover types were cotton and grapes, representing 10.2% (150 km^2) and 6 % (80 km^2) of the investigated domain, building/residential area 2.8 % (42 km^2), other vegetation 4.8 % (72 km^2), desert 75% (1117 km^2), unidentified 1.2 % (18 km^2).

Soil NO production and soil consumption rates, as well as the resulting net NO release rates from the top soil of wheat, corn, cotton, and jujube fields of the irrigated oasis agriculture (around the Taklimakan desert) have been characterized by Behrendt et al. (2014) and Mamtimin et al. (2015), respectively. The study by Mamtimin et al. (2015) has delivered evidence for a strong contribution of biogenic soil NO emission from these managed (irrigated, fertilized) dryland soils to the local total NO_2 budget. Having (a) the net potential NO flux (F_{NO} dependent on T_s and θ_v), (b) the surface soil temperatures (T_s), (c) the volumetric soil moisture contents (θ_v), and (d) the areal distribution of the three land use types (cotton, grapes, and desert) of the Tohsun oasis available, a 2D NO emission model was built with Arc GIS to determine the two dimensional biogenic soil NO emission source of the Tohsun oasis.

The raster data of the three most frequent land-cover types of the Tohsun oasis (cotton, grapes and desert) were implemented in the 2D soil NO emission model to quantify the NO emissions for each location. By that, the empirical relationship of soil NO emission to its driving parameters was used to upscale the laboratory estimates into two dimensions:

$$F_{NO}(x,y) = F_{NO}\left(\theta_{g,o}(x,y), T_{soil,0}\right) g\left(\theta_g(x,y)\right) h\left(T_{soil}(x,y)\right) \qquad (S12)$$

where $F_{NO}(x,y)$ is the land-use-type specific net potential NO flux, $\theta_g(x,y)$ and $T_{soil}(x,y)$ are the land-use-type specific gravimetric soil moisture content and soil temperature at the center of each grid point (30x30 m), $\theta_{g,0}(x,y)$ is the land-use-type specific, so-called optimum gravimetric soil moisture content (i.e., where the maximum NO release has been observed), and $T_{soil,0}$ is the reference temperature (here: 25°C; identical for all land-use types). The land-use-type specific exponential soil temperature curve $h\left(T_{soil,i}\right)$ and the land-use-type specific optimum soil moisture curve $g\left(\theta_{g,i}\right)$ are defined in the main text of the work (s. section 2.3.1).

In terms of data handling, an important requirement for modeling of the 2D NO emission is the accurate description of unique identifiers. Two identifiers have been attributed to each grid point (x,y), namely (a) the geographic coordinate (x, y of the center of each grid point of the corresponding pixel), and (b) the object ID number followed by a description of (i) the land-use-type, (ii) the land-use-type specific net potential NO flux, (iii) the land-use-type specific gravimetric soil moisture content, and (iv) the land-use-type specific soil temperature. Finally, land-use-type specific 2D NO emissions were calculated for the begin, the middle and the end of the vegetation period and are shown in Fig. S6. In the cotton fields a mean NO

emission of 0.003, 0.09, 0.006, 0.07, 0.004 and 0.004 ng m^{-2} s^{-1} (in terms of N) was observed in 25 April, 28 July, 13 August, 22 August, 06 September and 22 September, while the mean NO emissions in grape fields are 9.2, 39, 32, 18, 17, 12 ng m^{-2} s^{-1}, respectively. For the observation in April, the maximum NO emission (13 ng m^{-2} s^{-1},) was estimated from the grapes fields. With increasing soil temperatures, i.e. in the middle (July and August) and at end (September) of the growing period, maximum emissions (158, 128, 19 ng m^{-2} s^{-1}) have always been obtained for the grape fields. Although the grape fields of the Tohsun oasis receive less fertilizer than the cotton soils, highest mean NO emissions from grape soils are most likely due to the much higher soil temperatures. The variation of soil temperature emphasized that the land surface temperatures were 35-55°C in grape fields, and 25-50°C in the cotton fields in July (s. above). Additionally, the grapes' canopy provides only marginal shade to the soil while lower skin temperatures of the cotton fields were due to (a) effective shading of the soil by the fully developed cotton canopy which is considerably more dense than that of the grapes, and (b) transpiration of the cotton leaves which are known for highest transpiration rates. Consequently, the high soil temperature of grape fields will cause much higher NO emissions even throughout the growing period where was less difference between the gravimetric soil moisture content in the cotton and the grape fields. Particularly in July, grapes fields seem to have stored similar amounts of available water to the cotton fields: corresponding θ_g–values of cotton fields were between 0.167–0.33, and between 0.085–0.25 for the grape fields (s. Fig. S5). Summing up the 2010 NO emission rates (in terms of N) for the entire oasis, the corresponding totals (observations at the mentioned particular days in April, July, August, and September) are 610 g s^{-1}. The corresponding 2010 "seasonal" data are 45 (25 April), 188 (28 July), 152 (13 August), 87 (21 August), 80 (06 September) and 58 g s^{-1} (22 September), for oasis soils (grapes+cotton), while the corresponding data for "desert soils" are assumed to be independent of "season" (1.4 ± 0.46 g s^{-1}).

S2. Validation and calibration of satellite-derived surface temperature and soil moisture data

Six Landsat images of sufficient quality (cloud free observation) were available during our observation period in 2010, namely those of 25 April, (10:40 LT), 28 July (10:40 LT), 13 August (10:35 LT), 21 August (10:35 LT), 06 September (10:35 LT), and 22 September (10:35 LT). Since only one soil sensor has been buried at the Tohsun oasis during this period (2.5 cm depth; "bare soil"; Tohsun County Meteorological Station), validation of satellite-derived T_s (*LST*) and θ_g (*SMI*) data of Tohsun oasis could be realized only for the "desert"

land use type. For the bare soil of this site, the satellite-derived surface temperature ("skin temperature") represents the actual temperature at the soil surface (0 cm depth). Due to soil inertia (determined by the soil heat conductivity and capacity), any surface temperature signal needs a certain time period to propagate to deeper soil layers. From our measurements of the soil temperature profile (1, 2, 6, 10 cm depth) at the desert site of the Tohsun oasis, the time delay (surface to 2.5 cm depth) has been determined to 25 min. Consequently, for the intended validation of the satellite-derived T_s (*LST*) data, soil temperature measurements at Tohsun County Meteorological Station (5 min resolution) have been averaged (± 10 min) at a center time 25 min before the overflight of the satellite.

Behrendt et al. (unpublished data) provided the relationship between the relative humidity of soil air and the gravimetric soil water content (θ_g) based on laboratory calibration by a vapor sorption analyzer on soil samples from the Taklimakan desert. For the intended validation of satellite-derived θ_g (*SMI*) data, the soil air relative humidity measurements at the Tohsun County Meteorological Station (5 min resolution) have been averaged (± 10 min) at the respective overflight time of the satellite.

Satellite-derived land surface temperature data (*LST*) and gravimetric soil moisture content data (θ_g, derived from SMI) and the results of the corresponding *in-situ* data are shown in Fig. S4 a and b for the five Landsat images (28 July, 13 and 21 August, 06 and 22 September, 2010), which were available during the time period of our *in-situ* measurements (July – September 2010). There is a very good agreement between the satellite and *in-situ* surface temperature data as corresponding statistical tests indicated (error± 5%). In the case of gravimetric soil moisture content, there is also no significant difference between satellite derived and *in-situ* measured data considering the given errors of both data sets. However, it has to be noted, that this validation has been performed for a desert-like soil with an extremely low gravimetric soil water content (< 0.004).

S3. Data assimilation

"Data assimilation" is believed to be the correct "state-of-the-art"-term, if sources of different "source quality" are considered.

The intended comparison of (a) bottom-up with top-down estimates of Tohsun oasis' total NO_x emissions, and well as (b) soil biogenic emissions and anthropogenic emissions from Tohsun oasis confronted us with problems of (a) data availability in general, (b) in-completeness of available data, (c) very different temporal scales of existing data, and (d) to

find the common, reconciled temporal scale for the comparison. Finally, the temporal scale of available data to infer anthropogenic NO_X emissions as well as total NO_X emissions from satellite observations forced us to decide for the common and reconciled seasonal (monthly) temporal scale. However, calculating mean monthly land use type specific soil emissions from mean monthly data of soil temperature and gravimetric soil moisture content (according eqs. 2–4) seems inappropriate due to (a) the strongly non-linear response of the soil NO release from both variables, (b) large diel variations of the surface soil temperature (e.g. 10–60 °C; desert soil; July), and (c) large weekly variations of soil moisture caused by the applied irrigation schedules. Furthermore, fertilization application (usually concurrent with irrigation) leads to fertilizer amount and time dependent amplification of NO fluxes from the agriculturally managed oases soils. Consequently, the mean monthly land use type specific soil NO emissions have to be averaged from data calculated by temporal up-scaling with high resolution (< 1 h). Data availability in general and in-completeness of available data, however, made it necessary to assimilate temporally high resolution data from other data sources of different temporal scales and spatial origin, as well as different data quality. Corresponding procedures for soil temperature, gravimetric soil moisture content, fertilizer effects, and the anthropogenic emissions of Tohsun oasis are given below.

S3.1 Soil temperature, T_{soil}

For temporal up-scaling and spatial adjustment of the three measured soil temperature data sets ("desert", "cotton fields", "grape fields"), the corresponding Landsat satellite-derived surface temperatures of 25 April, 28 July, 13 and 21 August, and 06 and 22 September, 2010 have been used. For temporal up-scaling, these Landsat satellite-derived surface temperature data (for “desert”, “cotton fields”, and “grape fields”) have been fitted by 3rd order polynomials with respect to the day of year (DOY) 2010 (see Fig. S7). As a result, land surface temperatures (at 10:45 LT; i.e. satellite overflight) for the Tohsun oasis’ land use types can be calculated for every individual day between 1 April and 30 September 2010.

Soil temperature measurements (5 min) for the land-use types “desert”, “cotton fields”, and “grape fields” are available only for the period 1 July to 30 September 2010. To obtain data sets suitable for the entire considered time period (April–September 2010), the following approach has been chosen. Each data point of a particular day has been normalized by the mean value observed at 10:45 LT (± 15 min), the time of the Landsat satellite overflight. A data set of mean diel variation (30 min) of these normalized soil temperatures (5 min) has

been created by averaging all respective data between 1 July–30 September, constituting the representative diel variation of the (normalized) soil temperature of the respective land use type valid for the entire growing period (see Fig. S8). The diel variation of soil temperatures of the land use types "desert", "cotton fields", and "grape fields" for every day of the growing period 2010 are obtained by multiplying the normalized soil temperature data with the respective land surface temperature of this particular day. Results of the land use type specific soil temperatures (30 min resolution) for the entire growing period of 2010 are shown in Fig. 6 of the main paper.

S3.2 Gravimetric soil moisture content, θ_g

During July-September 2010, soil sensors (MSR® 165 data logger; s. sect. 2.2) have been buried at 2.5 cm depth only at the site of Tohsun County Meteorological station (bare desert soil). Evaluation of this data set yielded a temporally quite constant, very low gravimetric soil moisture content of 0.0028, which has been adapted for the entire growing season (April-September 2010) for the Tohsun oasis' land use type "desert". During the growing period 2010, gravimetric soil moisture contents of the land use types "cotton soils" and "grape soils" of Tohsun oasis result entirely from applied irrigation amounts and schedules. Unfortunately, there are no corresponding official data on Tohsun oasis' irrigation, neither in terms of amount and schedule, nor in terms of "drying-out" shape functions or values of field capacity (FC, s. sect. S1.8). *In-situ* measurements of gravimetric soil moisture contents of the land use types "cotton soils" and "grape soils" were also lacking. Therefore, gravimetric soil moisture contents of both land use types had to be adapted from *in-situ* measurements at two comparable sites, Minfeng and Kuche oases (see sect. S1.8). At both locations, Frequency Domain Reflectometry (FDR) probes (ECHO-5, Decagon, USA) have been buried in irrigated cotton, and jujube fields during July-September 2010. Following the measurements of soil moisture (5min resolution) of the two sites, we found that due to the applied irrigation schedules the lower limit of the gravimetric soil moisture content ($\theta_{g,min}$) was never as low as that at conditions of the "permanent wilting point" (*PWP*, s. sect. S1.8). That means, regular irrigation always started long before unwanted permanent wilting conditions were reached. Instead, temporal variation of the gravimetric soil moisture content was observed as follows: starting from upper limits of $\theta_{g,max,jujube}$ at $1.5\times FC_{jujube}$ and $\theta_{g,max,cotton}$ at $1.75\times FC_{cotton}$ (equilibrating at the time of (flooding) irrigation), over $\theta_{g,jujube}$ at $1.0\times FC_{jujube}$ and $\theta_{g,cotton}$ at $1.0\times FC_{cotton}$ (equilibrating about 2.5–3.5 days after stop of irrigation), and ending at lower

limits $\theta_{g,min,jujube}$ at $0.25 \times FC_{jujube}$ and $\theta_{g,min,cotton}$ at $0.5 \times FC_{cotton}$ (after about 14 days, and shortly before the next irrigation cycle). We adapted these findings for the cotton and grape soils of the Tohsun oasis. Finally, we used the following $\theta_{g,min}$ and $\theta_{g,max}$ values for soil originating of the three land use types of Tohsun oasis: 0.167 and 0.586 for cotton soils, 0.086 and 0.514 for grape soils, and $\theta_{g,min} = \theta_{g,max} = 0.0028$ for desert soils. Results of the land use type specific gravimetric soil moisture contents (30 min resolution) for the entire growing period of 2010 are shown in Fig. S9.

S3.3 Fertilizer factor, *FF* and Q_{10}-factor, $Q_{10}F$

There is also no offcial precise information on Tohsun oasis' fertilizer rates and fertilization schedules. In Xinjiang as well as in Tohsun, the rate of fertilizer was usually applied according to the local farming regime, which varied greatly among the different farms (Chen et al., 2008). Therefore, for consideration of the fertilizer effect (i.e. the amplification of the net biogenic NO fluxes through fertilizer application), we followed the recommendations of the local agricultural administration (personal information, 2010) and our personal communication with farmers (2010). The first fertilization ("base fertilizer event") usually occurs in early April, applying 200 ± 50 kg(N)ha^{-1} to grape fields, and 310 ± 40 kg(N)ha^{-1} to cotton fields. During the rest of the growing period four more fertilizing events follow, namely at the end of May, mid of June, end of July, and beginning of August, with 20–35% of the "base fertilizer event" amount in May and June, and 50–60% in July and August. It is known, that the fertilizer effect on the emission of N-containing gases is temporally declining after a fertilization event (Chen et al., 2011). Consequently, the decline has been considered by the time-dependent, exponential decays of *FF* and $Q_{10}F$, starting with given, *FA*-dependent *FF*- and $Q_{10}F$ -values (according to Fechner (2014); s. sect. 2.3.3.3) six hours after the respective fertilization events, and ending with $FF = Q_{10}F = 1$ after 14 days. The latter event accounts for the common practice at the Taklimakan's oases that agriculturally managed fields receive fertilizer concurrently with (or even dissolved in) irrigation waters; the delay of six hours (after each fertilization event) accounts for equilibrating unavoidable disturbances during fertilization and/or irrigation events. The seasonal course of *FF*- and $Q_{10}F$ -values (30 min resolution) resulting from the described data assimilation is shown in Fig. S10.

S3.4 Anthropogenic NO_X emissions of Tohsun oasis

The calculation (bottom-up) anthropogenic NO_X emissions is based on NO_X emission factors (usually given in terms of NO_2) which are widely used in P.R. China (s. Table S1), while the calculation of the particular emitted mass (E^N; in kg NO_2) is based on the following equation:

$$E^N_{i,j(k),f}(t) = \left(1 - P^N_{i,j(k),f}(t)\right) * K^N_{i,j(k),f}(t) * F_{i,j(k),f}(t) \qquad (S13)$$

where P^N is the dimensionless removal efficiency of the emission reduction technology (if applied); K^N (in kg t^{-1}) is the emission factor (mass of emitted NO_X per mass of fuel, weighted as NO_2); F (in t) is the fuel consumption; the subscript "i" represents any autonomous region or province of P.R. China (here: Turpan County); the subscript "$j(k)$" is the emission source category in the economic sector "k"; the subscript "f" is the fuel type, and "t" is the time (year). Coal is the dominating fuel type of energy consumption (65% of total; Pu, 2011). Tohsun's heating system changed in 2007, the former inefficient central coal fired boiler was shut down and replaced by de-central heating systems. Most of the boilers of the central heating facilities were based on 'low NO_X burner technologies', which means that the potential coefficient of emission-reduction for coal-fired thermal power is equal to 0.67 (Zhou, 2006; Mao et al., 2012). For calculation of the emission factor of electric power, we multiplied the uncontrolled emission factors by that new removal efficiency coefficient. As mentioned in sect. 2.2, data of fossil fuel consumption from the different economic sectors of Tohsun County were only available on an annual basis. For down-scaling to mean monthly values, the particular mean monthly percentages of anthropogenic NO_2 emissions of Urumqi (140 km NNW of Tohsun) have been adapted for Tohsun oasis. These data were reported by Mamtimin et al. (2011) and read as follows: 0.148, 0.157, 0.125, 0.069, 0.041, 0.035, 0.031, 0.046, 0.051, 0.066, 0.099, and 0.132 for January to December, respectively.

Table S1. Emission factors for NO_x for individual source* categories and fuel types (in kg NO_2 t^{-1}) widely used in P.R. China (compilation of data given by Hao et al., 2002; Zhang et al., 2009; and Shi et al., 2014).

economic sector	coal	crude oil	coke	gasoline	natural gas	diesel
electric power	11.8	6.35	---	9.4	36.47	5.32
industry	7.5	5.3	9.0	16.7	24.0	9.62
domestic use	1.19	1.7	2.25	16.7	14.62	14.62
transportation	---	---	9.0	21.24	20.85	20.85
construction	7.5	---	9.0	16.7	20.85	20.85

* all emission factors are in kg NO_2 t^{-1}, except for natural gas, they are in 10^{-4} kg NO_2 m^{-3} (Pu, 2009 & 2011)

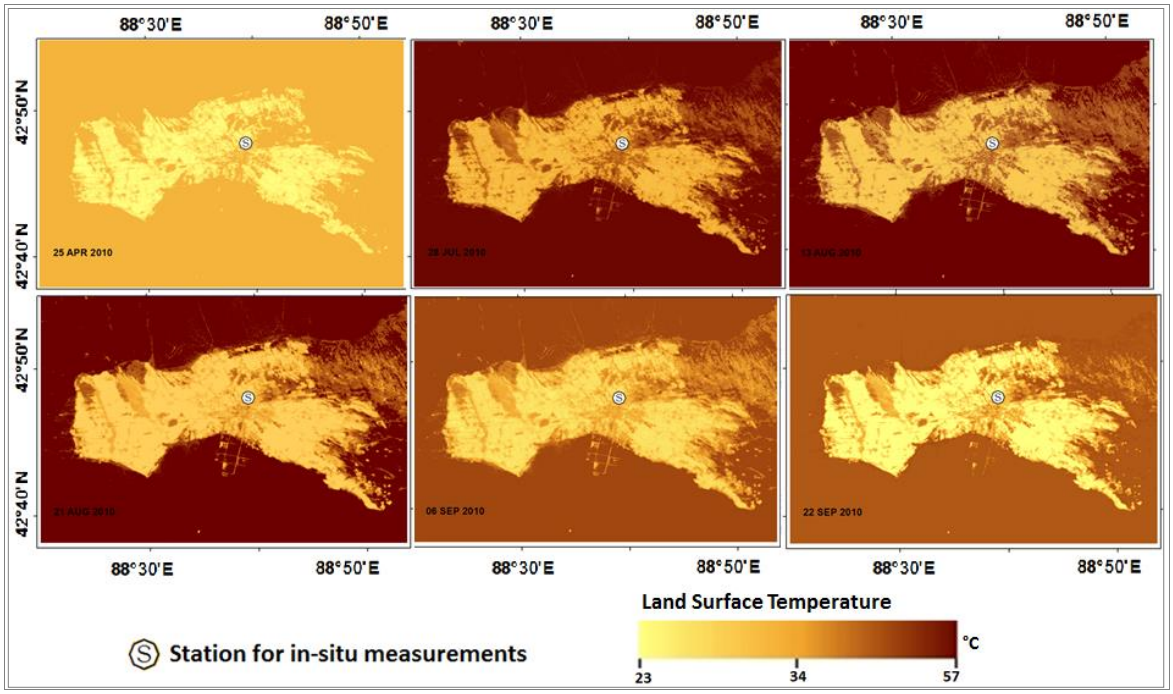

Fig. S1: 2D distributions of Land Surface Temperature (*LST*) of the Tohsun oasis derived from Landsat images (11:00 local time) of 25 April, 28 July, 13 August, 21 August, 06 September and 22 September 2010.

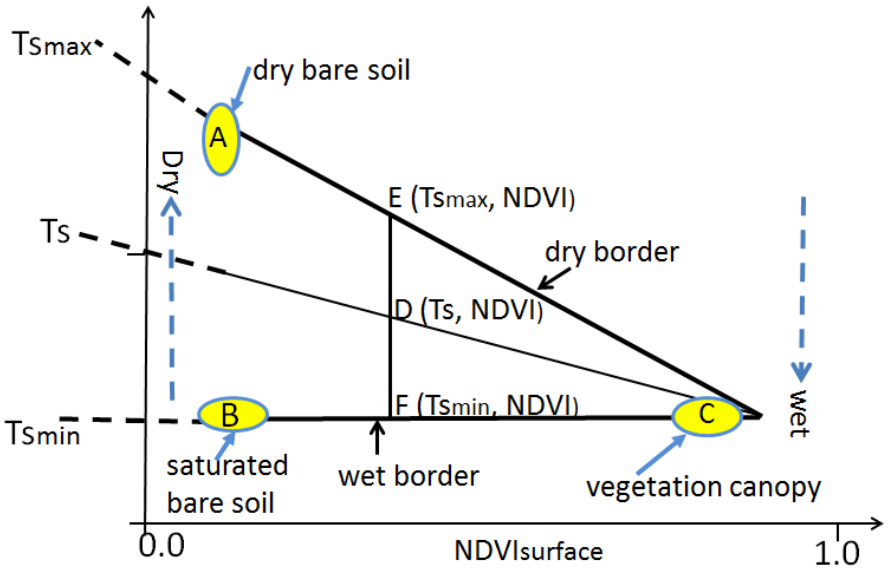

Fig. S2: Simplified representation of the $T_s/NDVI_{surface}$ space (a scatter space, when plotting T_s *vs*. the corresponding $NDIV_{surface}$ data) used for the calculation of the soil moisture index (*SMI*)

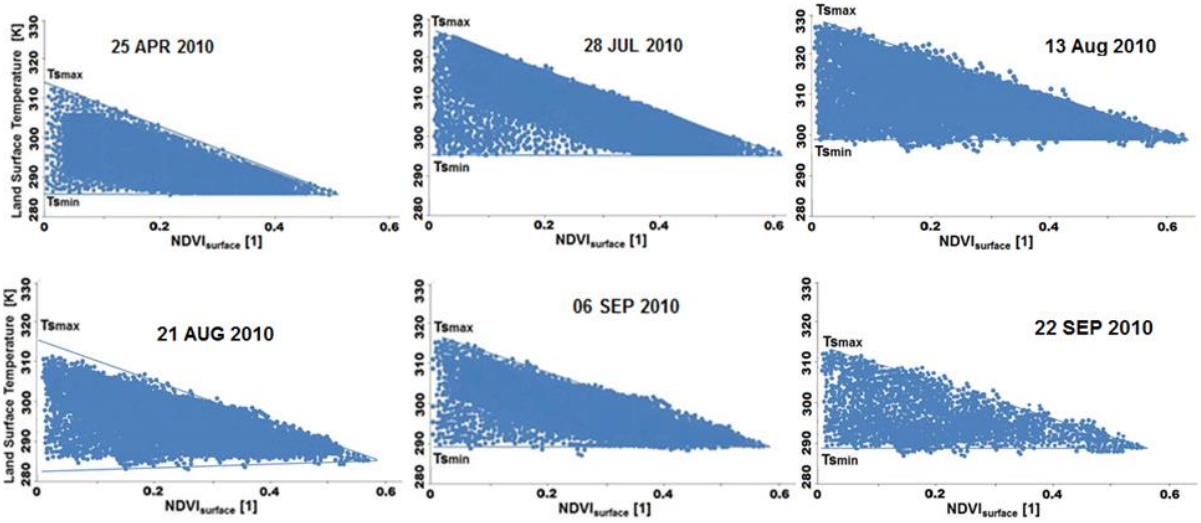

Fig. S3: Scatter plots of the Land Surface Temperature T_s *vs.* the Normalized Differenced Vegetation Index $NDVI_{surf}$ derived from Landsat images of the Tohsun oasis on 25 April (begin of the vegetation period), 28 July, 13 and 21 August, (middle of the vegetation period), and 06 and 22 September (end of the vegetation period).

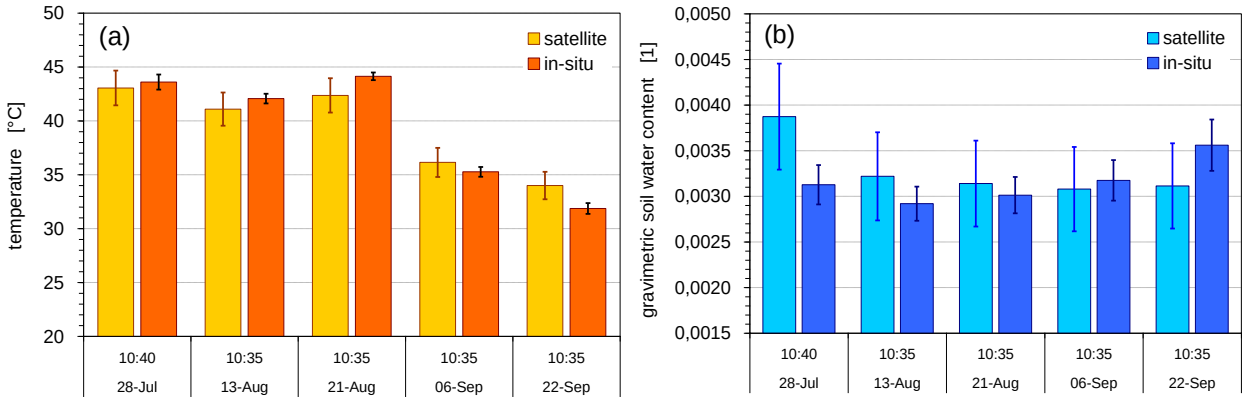

Fig. S4: Satellite-derived land surface temperature and gravimetric soil moisture content and results of *in-situ* measurements (soil temperature and relative humdity of soil air at 5 cm depth) in bare soil at Tohsun County Meteorological station during July–September 2010. *In-situ* data of relative humdity of soil air have been converted to gravimetric soil moisture content (by laboratory calibration, s. Sect. 2.4.6). Light color bars represent the Landsat satellite data (at local time of overflight), dark color bars indicate 20 min averages of the *in-situ* measurements (25 min time delay due to heat conductance is considered, s. Sect. 2.4.6). Error bars indicate the typical uncertainties of satellite-derived data (± 15%) and the instrumental uncertainty of the *in-situ* measurements (± 5% relative humidity of soil air), respectively.

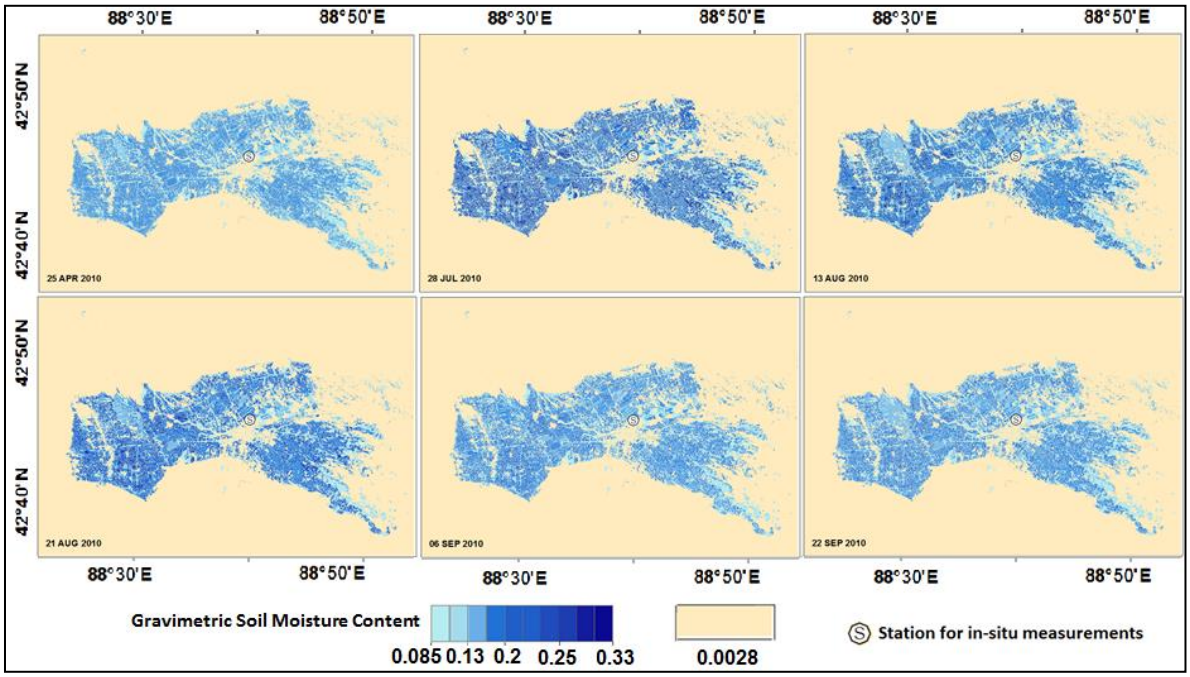

Fig. S5: 2D distributions of the gravimetric soil moisture content of the Tohsun oasis derived from Landsat images (11:00 local time) of 25 April, 28 July, 13 August, 21 August, 06 September and 22 September 2010.

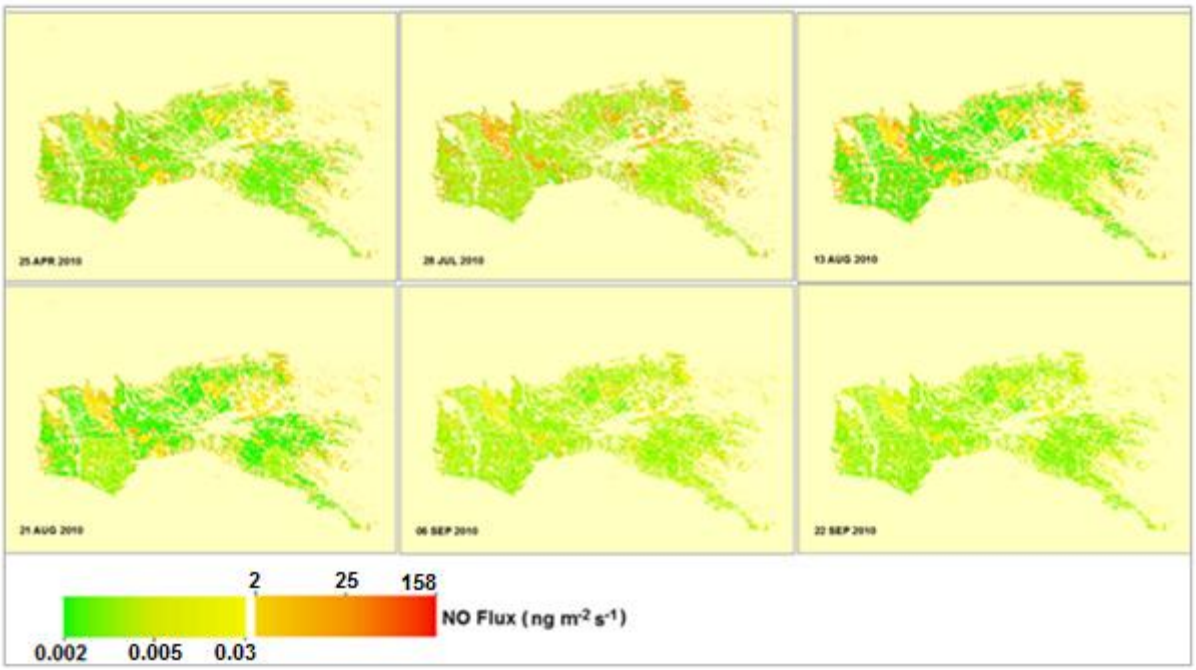

Fig. S6: Results of up-scaled biogenic NO emission from the Tohsun oasis (ng m^{-2} s^{-1}, in terms of N) for the beginning (25 April), the middle (28 July, 13 August, 21 August), and the end (06 September, 22 September) of the 2010 growing period.

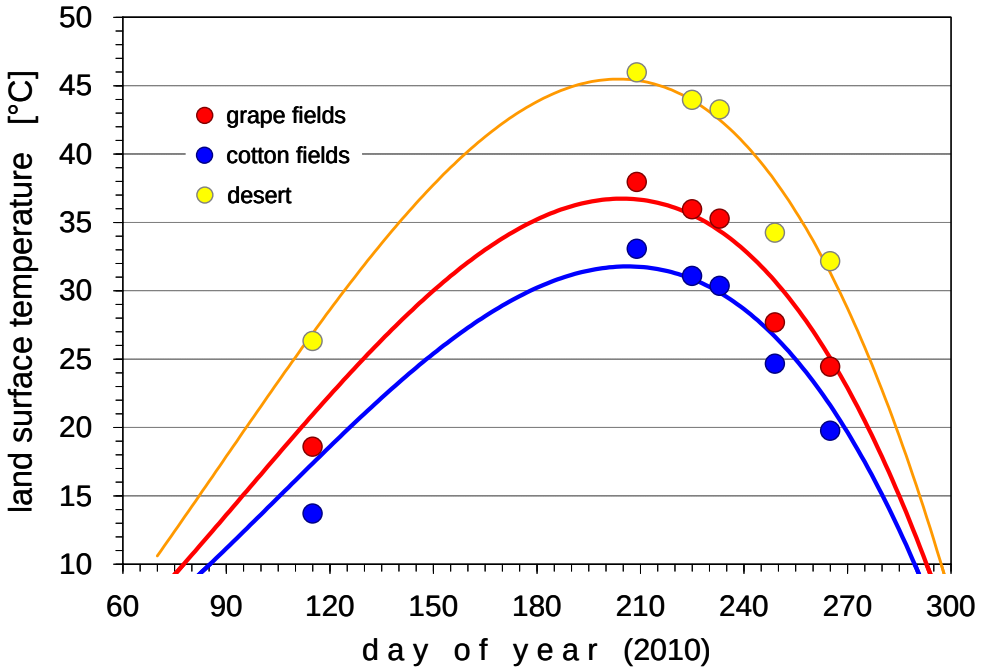

Fig. S7: Land surface temperature data for the three land-use types "desert", cotton fields", "grape fields" of the Tohsun oasis as derived from Landsat images on 25 April (DOY 115), 28 July (DOY 209), 13 (DOY 225) and 21 (DOY 233) August, 06 (DOY 249) and 22 (DOY 265) September, 2010 (approx. 10:45 LT). The corresponding curves represent 3rd order polynomial fits to the data (R^2 = 0.98, 0.96, and 1.00 for "grapes fields", cotton fields", "desert", respectively).

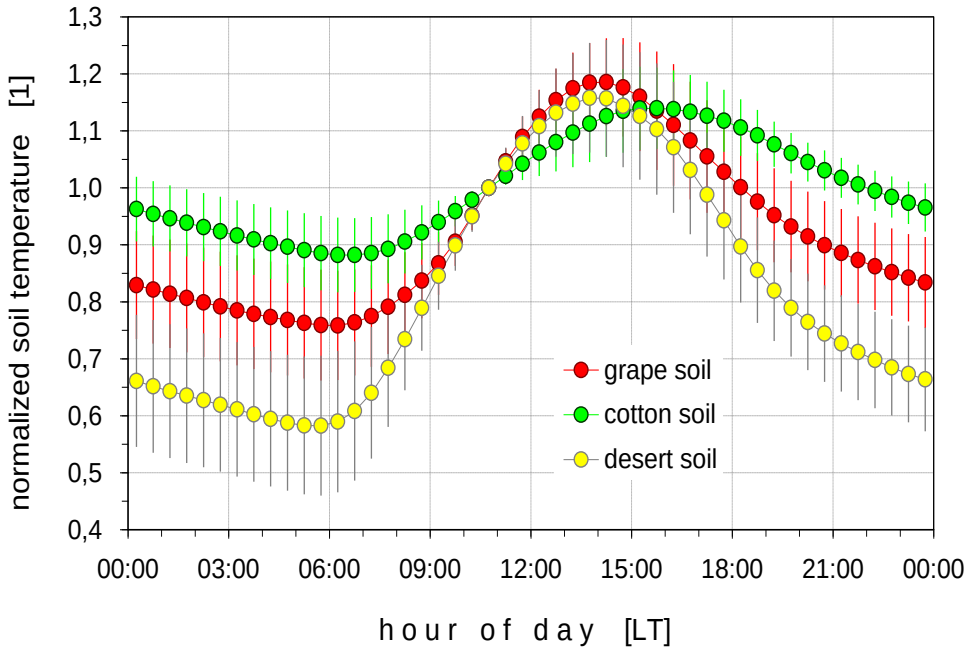

Fig. S8: Mean diel variation of the normalized soil temperatures (30 min averages) for the three land use types "desert", cotton fields", "grape fields" of the Tohsun oasis; original data (5 min) of every particular day have been normalized to the mean soil temperature observed at 10:45 LT (Landsat satellite overflight time).

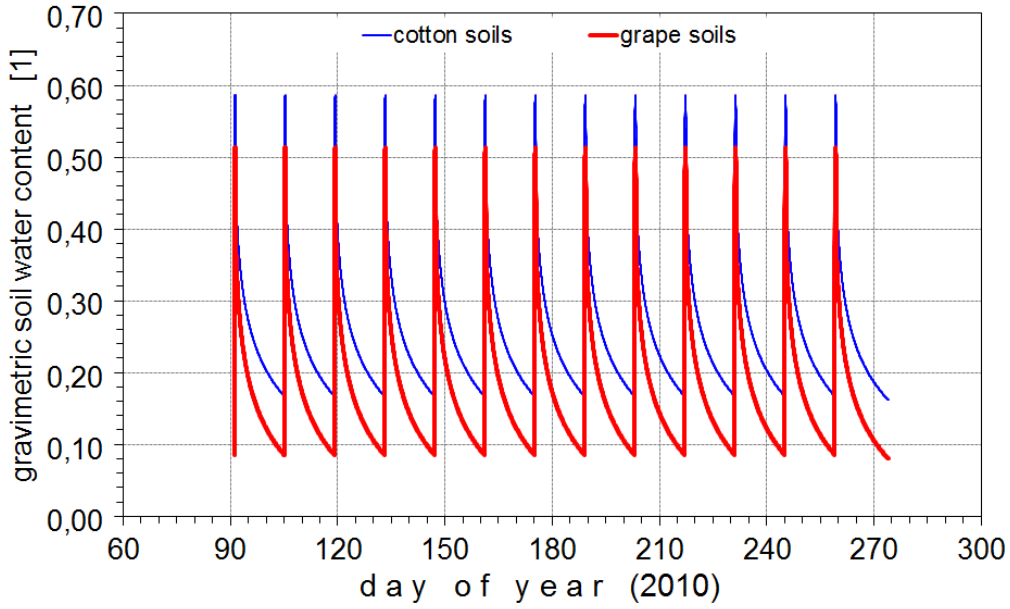

Fig. S9: Seasonal variation of the gravimetric soil moisture content (at 30 min resolution) for the land use types "cotton fields" and "grape fields" of the Tohsun oasis for the entire growing period of 2010 (01 April, DOY 90 – 30 September, DOY 273); regular temporal patterns are due to chosen irrigation schedules (starting at 01 April (DOY 90) and repeated every 2 weeks) adapted from observations at the oases of Kuche and Minfeng (details, s. text). Gravimetric soil moisture content for the land use type "desert" is assumed to be constant (0.0028).

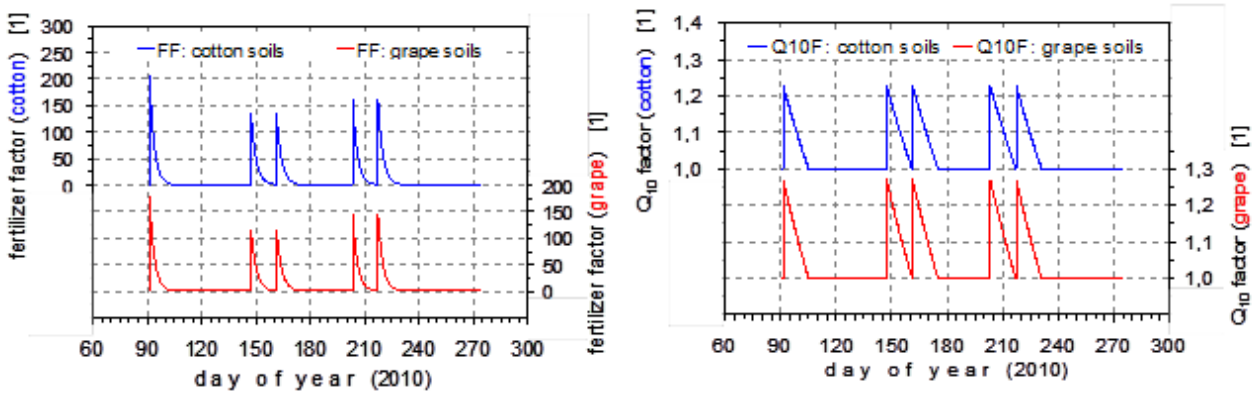

Fig. S10: Seasonal variation of the (dimensionless) factors FF (upper panel) and $Q_{10}F$ (lower panel; details s. text) which enhance the net NO fluxes of the land use types "cotton fields" and "grape fields" of the Tohsun oasis due to fertilizer application for the entire growing period of 2010 (01 April, DOY 90 – 30 September, DOY 273).

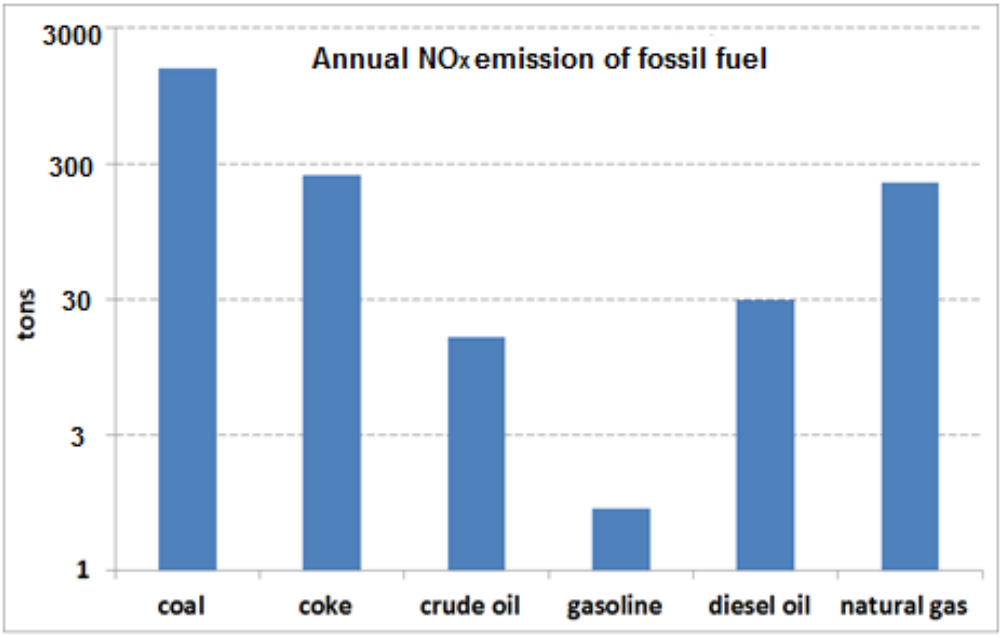

Fig. S11: Annual NO_X emission of fossil fuel of Tohsun County for 2010 (in terms of N)

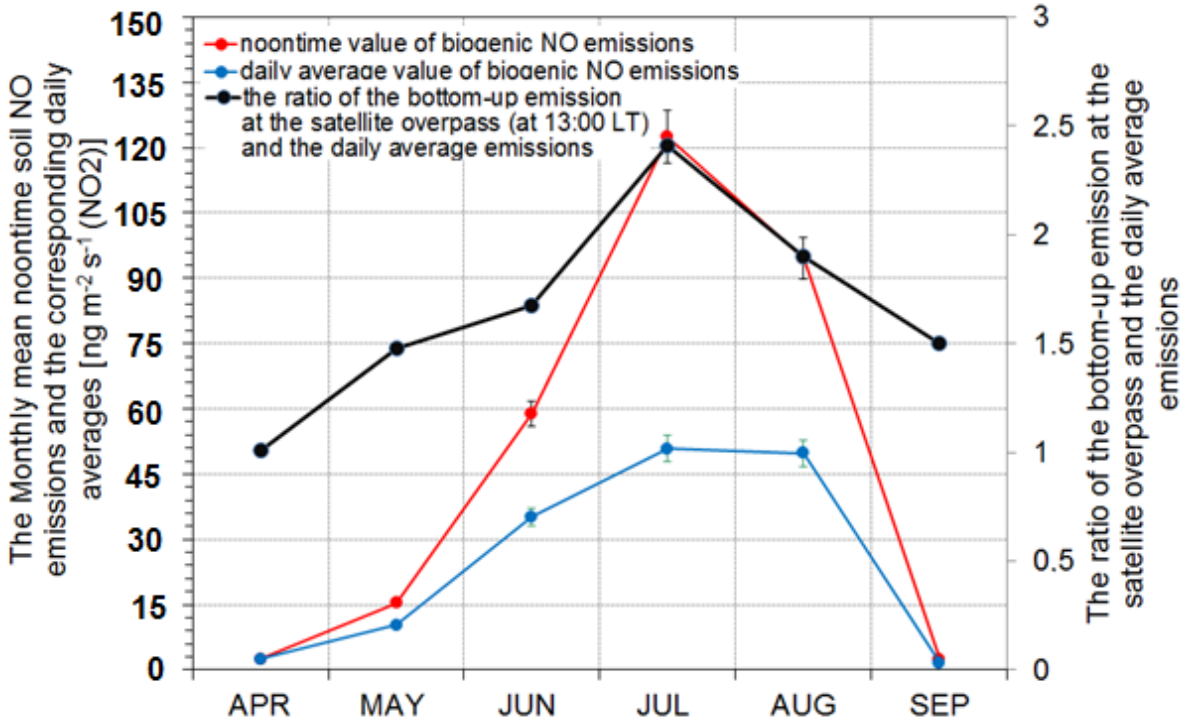

Fig. S12: Tohsun oasis biogenic NO emissions during the growing season for 2010: Monthly mean Noontime emissions, daily averages (all data are given in terms of mass of atomic Nitrogen) and the corresponding ratio (right axis).

References

Beck, R.: Scan Line Corrector -off Products Available. Landsat Project News October/November

2003. http://landsat.usgs.gov/project_news/October_November_2003.php, 2003.

Behrendt, T., Veres, P.R., Ashuri, F., Song, G., Flanz, M., Mamtimin, B., Bruse, M., Williams, J., and Meixner, F.X.: Characterisation of NO production and consumption: new insights by an improved laboratory dynamic chamber technique. Biogeosciences, 11, 5463–5492, doi:10.5194/bg-11-5463-2014, 2014.

Carlson, T., Gillies, R., and Schmugge, T.: An interpretation of methodologies for indirect measurement of soil water content. Agricultural and Forest Meteorology, 77,191-205, 1995.

Chander, G. and Markham, B.: Revised Landsat-5 TM radiometric Calibration procedures and postcalibration dynamic ranges. IEEE Transaction on Geoscience and Remote Sensing, Vol. 41, No. 11, 2674-2677, 2003.

Chander, G., B.L. Markham, B.L., and D.L. Helder.: Summary of current radiometric calibration coefficients for Landsat MSS, TM, ETM+, and EO-1 ALI sensors. Remote Sensing of Environment, Vol. 113-5, 893-903, 2009.

Chen, X.P., Cui, Z.L., Vitousek, P.M., Cassman, K.G., Matson, P.A., Bai, J.S., Meng. Q.F., Hou, P., Yue, S.C., Römheld, V., and Zhang, S.F.: Integrated soil-crop system management for food security. PNAS, Vol. 108-16, 6399-6404, 2011.

Du, Y., Teillet, P.M., and Cihlar, J.: Radiometric Normalization of Multitemporal High-resolution Satellite Images with Quality Control for Land Cover Change Detection. Remote Sensing Enviroment, 82, 123-134, 2002.

Goward, S., Xue, Y., and Czajkowski, K.: Evaluating land surface moisture conditions from the remotely sensed temperature/vegetation index measurements. An exploration with the simplified simple biosphere model. Remote Sensing of Environment, 79, 225-242, 2002.

Irish, R.: Landsat 7 Science Data Users Handbook, NASA Goddard Space Flight Cent., Greenbelt, Md. (Available at http://ltpwww.gsfc.nasa.gov/IAS/handbook/handbook_toc.html), 2003.

Jackson, T., Chen, D., Cosh, M., Li, F., Anderson, M., Walthall, C., Doriaswamy, P., and Hunt, E.: Vegetation water content mapping using Landsat data derived Normalized Difference Vegetation Index for corn and soybeans. Remote Sensing of Environment, 91, 475-482, 2004.

Jensen, J.R.: Introductory Digital Image Processing: A Remote Sensing Perspective. 3ndEdiiton, Prentice-Hall, Upper Saddle River, 198-210, 337- 401, 2005.

Lambine, E. F. and D. Ehrlich: The surface temperature-vegetation index space for land cover and land-cover change analysis. International Journal of Remote Sensing, 17, pp. 463-487,1996.

Mallick, K., Bhattacharya, B.K., and Patel, N.K.: Estimating volumetric surface moisture content for cropped soils using a soil wetness index based on surface temperature and NDVI. Agricultural and Forest Meteorology, 149, 1327–1342, 2009.

Mamtimin, B., Behrendt, T., Badawy, M.M., Wagner, T., Qi, Y., Wu, Z., and Meixner, F.X.: Tropospheric vertical column densities of NO2 over managed dryland ecosystems (Xinjiang, China): MAX-DOAS measurements vs. 3-D dispersion model simulations based on laboratory-derived NO emission from soil samples. Atmos. Chem. Phys., 15, 867–882, doi: 10.5194/acp-15-867-2015, 2015.

Markham, B. L., and Barker J. L.: Landsat MSS and TM postcalibration dynamic ranges, exoatmospheric reflectance and at-satellite temperatures, EOSAT Landsat Tech. Notes 1, pp. 3 – 8, Earth Obs. Satell. Co., Lanham, Md., 1986.

Sandholt, I., Rasmussen, K., and Andersen, J.: A simple interpretation of the surface temperature/vegetation index space for assessment of surface moisture status, Remote Sensing of Environment, 79, 213-22, 2002.

Schott, J. R., and Volchok, W. J.: Thematic Mapper thermal infrared calibration, Photogramm. Eng. Remote Sens., 51, 1351–1357, 1985.

Sobrino, J.A., Jiménez-Muñoz, J.C., and Paolini, L.: Land surface temperature retrieval from Landsat TM 5. Remote sensing of Environment 90, 434-440, 2004.

Storey, J., Scaramuzza, P., Schmidt, G., and Barsi, J.: Landsat 7 scan line corrector-off gap filled product development. In Proceeding of the 2005 American Society for Photogrammetry and Remote Sensing Pecora 16 Conference on Global Priorities in Land Remote Sensing, Sioux Falls. South Dakota, 2005.

Storey, C. J.: Landsat image geocorrection and registration, in: Image Registration for Remote Sensing, edited by: Le Moigne J., Netanyahu, N.S. and Eastman, R.D., Cambridge University Press, 400-414, 2011.

Van de Griend, A. A., and Owe, M.: On the relationship between thermal emissivity and the normalized difference vegetation index for natural surfaces. International journal of Remote Sensing, 14 (6), 1119-1131. Biogeosciences Discussions, 5, 4621–4680, 1993

Wang, X., Xie, H., Guan, H., and Zhou, X.: Different responses of MODIS-derived NDVI to Root-zone soil moisture in semi-arid and humid regions. Journal of Hydrology, 340, 11-24, 2007.

Yilmaz, M., Hunt Jr., E., Goins,L., Ustin, S., Vanderbilt, V., and Jackson, T.:Vegetation water content during SMEX04 from ground data and Landsat 5 Thematic Mapper imagery. Rem ote Sensing of Environment, 112, 350-362, 2008.

Wagner, W., Lemoine, G., and Rott, H.: A method for estimating soil moisture from ERS scatterometer and soil data. Remote Sensing and Environment, 70, 191-207, 1999.

Zeng, Y., Feng, Z., and Xiang, N.: Assessment of soil moisture using Landsat ETM+ temperature/vegetation index in semiarid environment. IEEE, 4306-4309, 2004.